

A Highly Efficient and Durable Air Electrode for Intermediate-temperature Reversible Solid Oxide Cells

Weilin Zhang,^{a, †} Yucun Zhou,^{a, †} Enzo Liu,^{a, c} Yong Ding,^a Zheyu Luo,^a Tongtong Li,^a Nicholas Kane,^a Bote Zhao,^a Yinghua Niu,^a Ying Liu,^b and Meilin Liu,^{a, *}

a. School of Materials Science and Engineering, Georgia Institute of Technology, 771 Ferst Dr. NW, Atlanta, GA, 30332-0245, USA.

b. Phillips 66 Company, 2331 CityWest Blvd., Houston, TX, 77042.

c. School of Materials Science and Engineering, Tianjin University, Tianjin 300350, China.

* Corresponding author. Email address: meilin.liu@mse.gatech.edu

† These authors contributed equally.

Abstract

Solid oxide cells (SOCs) are considered the most efficient system for reversible conversion between chemical and electrical energy, thus having potential to be an attractive technology for a sustainable energy future. To achieve high round-trip efficiency, highly efficient and durable air electrode materials are needed to minimize energy loss associated with oxygen reduction reaction (ORR) and oxygen evolution reaction (OER). Here we report a bi-functional air electrode material, $\text{PrBa}_{0.9}\text{CO}_{1.96}\text{Nb}_{0.04}\text{O}_{5+\delta}$, demonstrating outstanding electrochemical performance (e.g., achieving peak power densities of over 1.5 and 1 W cm^{-2} , respectively, for $\text{Gd}_{0.1}\text{Ce}_{0.9}\text{O}_{1.95}$ and $\text{BaZr}_{0.1}\text{Ce}_{0.7}\text{Y}_{0.1}\text{Yb}_{0.1}\text{O}_{3-\delta}$ based fuel cells at 600 °C) while maintaining excellent stability (e.g., having a degradation rate of 40 mV per 1,000 h for H_2O electrolysis cells). The excellent property of the new electrode is attributed to the improved stability from Nb doping and the enhanced electrocatalytic activity from tuning Ba deficiency, as confirmed by experimental results and computational analysis.

Keywords: reversible solid oxide cells, hydrogen production, energy conversion, air electrode

1. Introduction

The increasing demand for clean energy and the rapid growth in solar- and wind- based electricity generation require highly efficient and reliable energy conversion and storage devices for long-term and large-scale applications. Solid oxide cells (SOCs), which can operate in both the fuel cell mode and the electrolysis cell mode, offer unique solutions for this energy challenge [1, 2]. When the electricity demand is high, an SOC can operate in the fuel cell mode to directly generate electricity from a wide variety of chemical fuels, from hydrogen to renewable fuels [3-5]. When excess electricity is available, the same SOC can operate in the electrolysis cell mode to produce fuels through electrolysis of water (to generate hydrogen) or carbon dioxide (to synthesize carbon-containing fuels) [6-8]. Thus, reversible operation of SOCs allows direct conversion between chemical energy and electrical energy with high roundtrip efficiency at low cost, offering a promising solution to a clean and sustainable energy future. Despite the unique advantages offered by SOCs, large-scale commercialization of SOCs remains challenging due to the lack of highly active and robust air electrode materials at intermediate temperatures (~ 600 °C). An ideal air electrode material for SOCs should have outstanding electrocatalytic activities for the oxygen reduction reaction (ORR) and the oxygen evolution reaction (OER), good electrochemical stability in both dry and humidified air, and good chemical and physical compatibility with the electrolyte material and other cell components [9-13]. As a mixed ionic and electronic conductor, $\text{La}_{0.6}\text{Sr}_{0.4}\text{Co}_{0.2}\text{Fe}_{0.8}\text{O}_{3-\delta}$ (LSCF) has been widely used as an air electrode material, but the relatively low catalytic activity and poor stability due to Sr segregation prevent its use in long term applications [14]. Double perovskites, such as $\text{PrBaCo}_2\text{O}_{5+\delta}$ (PBCO), exhibits excellent oxygen ion conductivity, however, the long-term stability is still vulnerable to cation segregation under operating conditions [15-17]. In recent years, several breakthroughs on air electrodes have been made for different applications, including highly active cathodes for solid oxide fuel cells (SOFCs) [18-20], multiphase nanocomposites for protonic ceramic fuel cells (PCFCs) [21], and triple conducting materials for protonic ceramic electrolysis cells (PCECs) or reversible protonic

ceramic electrochemical cells (RePCECs) [6-8]. However, very few studies report a bi-functional air electrode material applicable to different types of SOCs and the guiding principles for rational design of better air electrode materials are still missing. Additionally, the overall performance and stability of the existing SOCs still need further enhancement for practical applications. Here we report our findings in fabrication, characterization, and application of a new bi-functional air electrode material, $\text{PrBa}_{0.9}\text{Co}_{1.96}\text{Nb}_{0.04}\text{O}_{5+\delta}$ (PB9CN), which displays excellent electrocatalytic activity, durability, and applicability to reversible SOCs. Through a step-by-step optimization procedure, we have demonstrated that the stability can be significantly enhanced via altering Nb doping while electrocatalytic activity being boosted via tuning Ba deficiency. $\text{Sm}_{0.2}\text{Ce}_{0.8}\text{O}_{1.9}$ (SDC) and $\text{BaZr}_{0.1}\text{Ce}_{0.7}\text{Y}_{0.1}\text{Yb}_{0.1}\text{O}_{3-\delta}$ (BZCYYb) based symmetrical cells were used to demonstrate the excellent stability in both dry and humidified air for over 1000 hours. The outstanding electrochemical properties were further confirmed using $\text{Gd}_{0.1}\text{Ce}_{0.9}\text{O}_{1.95}$ (GDC), BZCYYb, and YSZ (8% $\text{Y}_2\text{O}_3\text{-ZrO}_2$) based single cells under typical operating conditions. For example, a GDC-based fuel cell achieved a peak power density of over 1.5 W cm^{-2} at $600 \text{ }^\circ\text{C}$. For a BZCYYb-based cell, a peak power density of 1.0 W cm^{-2} was achieved in the fuel cell mode, and a current density of 1.7 A cm^{-2} was demonstrated at 1.3 V in the H_2O electrolysis cell mode at $600 \text{ }^\circ\text{C}$. Moreover, the electrolysis cell showed excellent stability for over 1000 hours. These results clearly demonstrate the potential of the bi-functional air electrode material for highly efficient energy conversion and storage devices.

2. Experimental Section

2.1. Air electrode powder synthesis

$\text{PrBa}_{0.9}\text{Co}_{1.96}\text{Nb}_{0.04}\text{O}_{5+\delta}$ (PB9CN), $\text{PrBaCo}_{1.96}\text{Nb}_{0.04}\text{O}_{5+\delta}$ (PB10CN) and $\text{PrBaCo}_2\text{O}_{5+\delta}$ (PBCO) powder were synthesized by the sol-gel method. A stoichiometric amount of metal nitrates were dissolved in DI water with ethylenediaminetetraacetic acid (EDTA) and citric acid (CA). The molar ratio between the metal ions, EDTA, and CA was 1:1:1.5. Ammonium hydroxide was used to adjust the pH to about 9.

After evaporating the water, the gel was calcined at 250 °C for 10 hours. The primary powder was then grounded and calcined at 600 °C for 5 hours. Finally, the powder was fired at 1100 °C for 2 hours to form the desired phase, as confirmed by X-ray diffraction (XRD).

2.2. Fabrication of symmetrical cells and single cells

To fabricate symmetrical cells, SDC or BZCYYb powder was mixed with ≈ 1 wt.% Polyvinyl Butyral (PVB) then dry pressed and sintered at 1450 °C for 5 hours. PB9CN, PB10CN, and PBCO ink (air electrode powder mixed with V-006) were brush painted on both sides of the electrolyte followed by firing at 950 °C for 2 hours. To fabricate single cells, Ni-GDC|GDC and Ni-BZCYYb|BZCYYb bi-layers were prepared by co-tape casting and sintering at 1450 °C for 5 hours. For the YSZ based single cells, Ni-YSZ/YSZ bi-layers were prepared by co-tape casting and sintering at 1450 °C for 5 hours. Then a GDC buffer layer was drop coated on the surface of the YSZ electrolyte, followed by firing at 1250 °C for 2 hours. The air electrode ink was brush painted on the half cells or GDC buffer layer and fired at 950 °C for 2 hours. The effective area of the symmetrical cells and single cells was about 0.28 cm². YSZ-based 1-inch cells with an effective area of 1.13 cm² were also fabricated with the same method.

2.3. Electrochemical measurements

For symmetrical cells with two identical cathode materials, a piece of silver mesh covering the active electrode area was used as the current collector. Electrochemical impedance spectra (EIS) were acquired using a Solartron 1255 HF frequency response analyzer interfaced with an EG&G PAR potentiostat model 273A with an AC amplitude of 10 mV in the frequency range from 100 kHz to 0.01 Hz. The stability test was performed at 600 and 550 °C under the OCV condition in dry air or wet air (3 vol% H₂O). The SDC-based symmetrical cells were tested in stagnant air. The BZCYYb based symmetrical cells were tested in humidified air at a flow rate of 50 sccm. For the electrochemical testing of the BZCYYb based electrolysis cells, wet hydrogen (3 vol% H₂O) was supplied to the fuel electrode at a flow rate of 20 sccm and humidified air was supplied to the air electrode at a flow rate of 200 sccm. The cell performance was monitored with an Arbin multi-channel electrochemical testing system.

2.4. Other characterizations

The phase structure of air electrode powders were characterized by X-ray diffraction (Panalytical XPert PRO Alpha-1 XRD). The microstructure and morphology of the cells were examined by a scanning electron microscope (SEM, LEO 1530). The Nb content of the PB9CN powder and the elemental distribution at the surface of PBCO and PB10CN were characterized by a scanning transmission electron microscope (STEM, Hitachi HD-2700). The surface kinetic coefficient (k) and chemical diffusion coefficient (D) were characterized using the electrical conductivity relaxation (ECR) measurement. Oxygen non-stoichiometry was determined by a combination of iodometric titration at room temperature and thermogravimetric analysis (TGA) at elevated temperatures.

2.5. Computational method

The Vienna ab initio simulation package (VASP) was used for theoretical calculations. The interactions between the valence electrons and ion core was described by projector augmented wave (PAW) formalism of density functional theory [22]. The exchange correlation functional was depicted by the spin-polarized generalized gradient approximation proposed by Perdew, Burke, and Ernzerhof (PBE) [23]. The Gaussian smearing method was used [24], and the width of smearing was chosen to be 0.05 eV. The plane wave base used a kinetic energy cutoff of 400 eV. The Monkhorst-Pack k-point grid was used for sampling the Brillouin region with a k-point mesh of $7 \times 7 \times 7$ for the bulk calculation and $5 \times 5 \times 1$ for the surface model [25]. The bulk models are shown in Figure S1a and S1b, with a size of $8.00 \text{ \AA} \times 7.76 \text{ \AA} \times 7.63 \text{ \AA}$, containing 4 Pr, 4 Ba, 8 Co, and 24 O atoms. After one Co atom is replaced by Nb, the supercell size was $7.94 \text{ \AA} \times 7.83 \text{ \AA} \times 7.74 \text{ \AA}$, with the volume slightly increased. The surface slab model is shown in Figure S1e and S1f, with seven atomic layers, and a lateral size of $8.00 \text{ \AA} \times 7.63 \text{ \AA}$. For the geometry optimizations of the bulk, the volume of the supercell and all the internal coordinates were allowed to be relaxed, until the force on each atom was less than 0.01 eV/\AA . For the surface model, the bottom two atomic layers were fixed, and the other atoms were allowed to relax. The self-consistent convergence criterion for the calculation of the ground state energy was less than 10^{-5} eV .

3. Results and discussion

3.1. Structure of PB9CN

Three different air electrode materials, $\text{PrBa}_{0.9}\text{Co}_{1.96}\text{Nb}_{0.04}\text{O}_{5+\delta}$ (PB9CN), $\text{PrBaCo}_{1.96}\text{Nb}_{0.04}\text{O}_{5+\delta}$ (PB10CN), and $\text{PrBaCo}_2\text{O}_{5+\delta}$ (PBCO), were synthesized and compared in this study. Figure 1a shows a schematic view of the crystal structure of PBCO with Nb doping and Ba deficiency. Compared to the crystal structure of PBCO, Nb is doped into the Co site to create PB10CN. Additionally, 10% Ba deficiency is created to obtain PB9CN. PB9CN shows a double perovskite structure as confirmed by the X-ray diffraction (XRD) in Figure 1b, the high-angle annular dark-field (HAADF) image in Figure 1c, and the selected area diffraction (SAED) pattern in Figure 1d. The distance between PrO and BaO planes is about 0.766 nm, which is consistent with the XRD refinement result (Figure S2). The layered $[\text{Co}(\text{Nb})\text{O}_2]$ - $[\text{PrO}]$ - $[\text{Co}(\text{Nb})\text{O}_2]$ - $[\text{BaO}]$ structure and the Ba deficiency are vital to the rapid transport of oxygen species [26-28]. The content of Nb as the B-site ion is 2%, as determined using Energy-dispersive X-ray spectroscopy (EDS) as shown in Figure S3. Further increase in the concentration of Nb doping or Ba deficiency resulted in the formation of secondary phases (Figure S4).

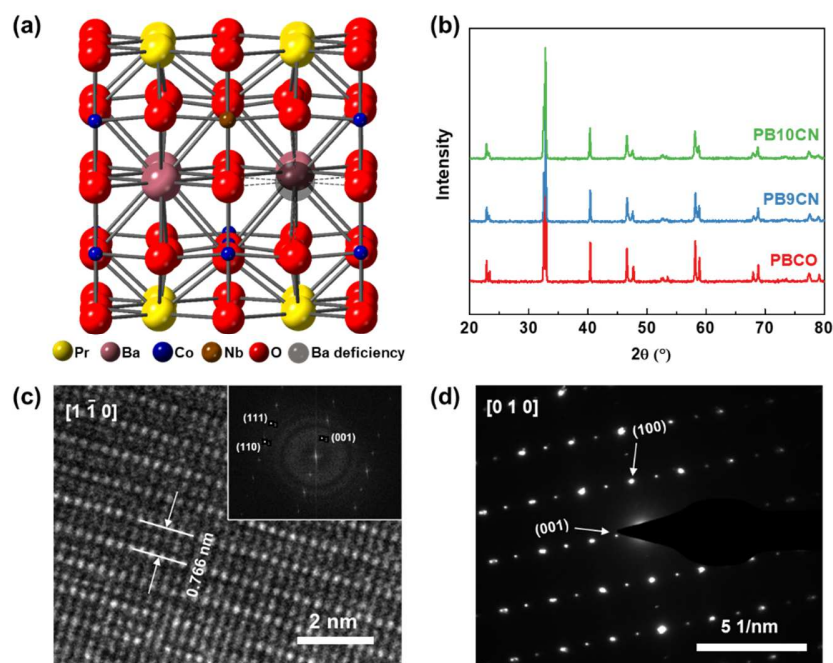


Figure 1. Crystal Structure of PB9CN. (a) Schematics of the PBCO crystal structure with Nb doping and Ba deficiency. (b) XRD patterns of PB9CN, PB10CN, and PBCO. (c) High resolution STEM image of PB9CN lattice (inset: fast Fourier transform pattern along the [1 -1 0] zone axis of PB9CN). (d) SAED pattern of PB9CN along the [0 1 0] zone axis.

3.2. Enhanced Stability by Nb Doping

Double perovskite PBCO shows fast oxygen transport properties, which makes it a good candidate for the air electrode in SOFCs [29]. However, due to cation segregation, the stability of PBCO is questionable and hardly reported [15, 16, 30]. To suppress the cation segregation, Nb was doped into the PBCO crystal structure to create PB10CN, the XRD pattern of both PBCO and PB10CN were shown in Figure 1b [31].

The electrochemical stability of PB10CN and PBCO were first investigated on SDC-based symmetrical cells. Figure 2a compares the change of interfacial polarization resistance (R_p) of both electrodes at 600 °C in ambient air under open circuit voltage (OCV) conditions. While the initial R_p of the two cells with different electrodes (PB10CN and PBCO) were similar (Figure S5), the R_p of the cell with the PBCO electrode increased much faster, with an increase of 20% after 200 hours. In contrast, the R_p of the cell with PB10CN increased only ~4%. The ohmic resistance (R_{ohm}) of the PBCO | SDC | PBCO symmetrical cell remained relatively constant during the 200 h testing (Figure S6), implying that the electrical contact between the electrodes and the electrolyte was stable. Thus, the increase in R_p of the cell with the PBCO electrode is attributed to Ba segregation as opposed to delamination of the electrode from the electrolyte. After the stability test, precipitated particles were seen on the surface of the PBCO electrode. In contrast, the surface of the PB10CN electrode remained clean (Figure S7). In order to get a better view of the precipitated particles, dense PB10CN and PBCO pellets were prepared. After polishing the surface (Figure S8), the pellets were annealed at 600 °C for 20 hours. After annealing, the surface of PB10CN did not show any obvious change, while the surface of the PBCO pellet showed precipitated particles, as compared in Figure 2b and 2c. These results support the observations of the porous electrodes. The precipitated particles at the surface of the PBCO pellet were

characterized using a scanning transmission electron microscope (STEM). Figure 2d and 2e show the STEM image and elemental distribution generated using an EDS line scan of the precipitated particle on the surface of the PBCO pellet, which illustrates that Ba segregation took place on PBCO during the annealing process [16, 30]. The bulk part of PBCO maintains the double perovskite structure. In contrast, with Nb doping, such segregation was successfully suppressed as the elemental distribution was uniform from the bulk to the surface in the PB10CN pellet (Figure S9), which contributed to the enhanced electrochemical stability. Similar behaviour was also observed for annealed PBCO and PB10CN powder samples. Even though no obvious secondary phase was identified by XRD (Figure S10), STEM analysis confirmed Ba segregation on PBCO powder sample (Figure S11 and S12). The enhanced stability by Nb-doping has been further confirmed by the stable operation of the PB10CN air electrode on a GDC-based single cell as shown in Figure S14.

To gain a molecular-level understanding of the enhancement of stability by Nb doping, we resorted to density functional theory (DFT) based calculations to estimate the cohesive energy and the formation energy of PBCO without (Figure S1a) and with Nb doping (Figure S1b). The cohesive energy is defined as $E_c = E_T - \sum_i n_i E_i$, where E_T is the total energy of the system, E_i is the energy of an isolated atom i , and n_i is the number of atom i in the system. The formation energy is defined as $E_f = E_T - \sum_j n_j E_j$, where E_T is the total energy of the system, E_j is the energy of atom j in its corresponding bulk, and n_j is the number of atom j in the system. As shown in Figure 2f, the cohesive energy and formation energy of the Nb doped model are 8.85 eV and 6.97 eV higher than those of the undoped system, indicating a more stable structure by Nb doping. Figure S1c and S1d show that the Nb doping can transfer more electrons from the metal ions to oxygen ions, which improves structural stability. The surface segregation energy of Ba was also calculated, which is defined as the energy difference between the Ba segregated model and the un-segregated model (Figure S1e and S1f for Nb doped system). Compared to the undoped

system, Nb doping increased the Ba segregation energy by 0.30 eV. This result is consistent with the enhanced cohesive and formation energies by Nb doping, as well as the electronic structure analysis.

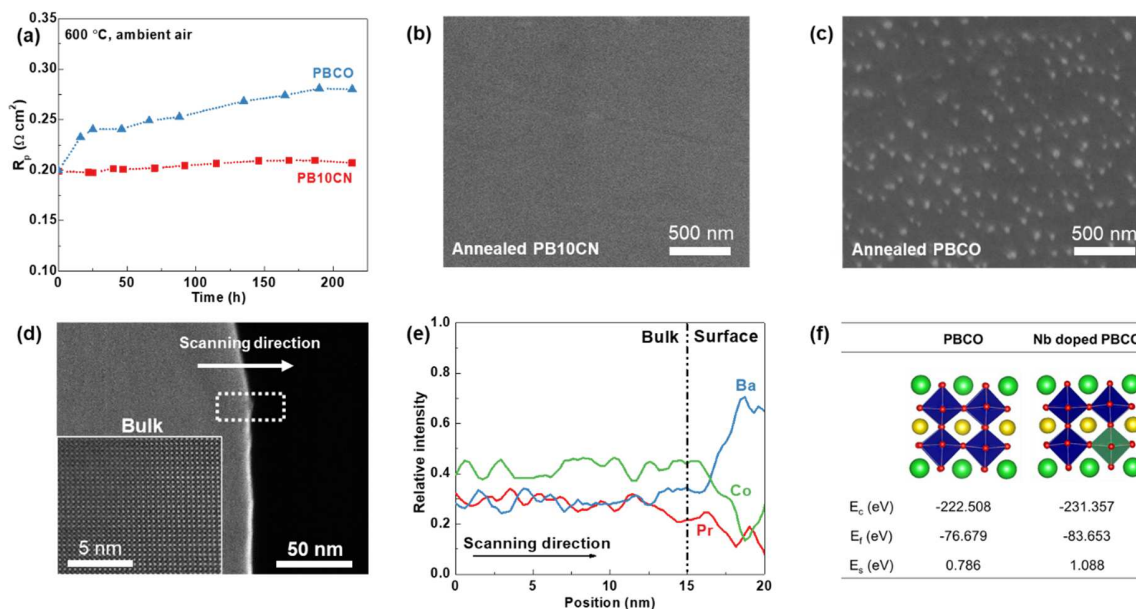


Figure 2. Enhanced Stability by Nb Doping. (a) R_p of PB10CN and PBCO as a function of time at 600 °C. (b) SEM image of surface of the annealed PB10CN pellet. (c) SEM image of surface of the annealed PBCO pellet. (d) STEM image of the cross-sectional view near the surface of the annealed PBCO pellet (inset: high resolution STEM image of the bulk PBCO after annealing). (e) EDS elemental distribution near the surface of the annealed PBCO pellet. (f) Cohesive energy (E_c), formation energy (E_f), Ba segregation energy (E_s) comparison between PBCO and Nb-doped PBCO.

3.3. Improved Electrocatalytic Activity by Tuning Ba Deficiency

Creating cation deficiency is an effective method to improve the electrochemical performance of air electrode materials [28, 32, 33]. By introducing Ba deficiencies (V_{Ba}''), more electron holes (h^\bullet) and/or oxygen vacancies ($V_{O^{\bullet\bullet}}$) are generated to maintain charge neutrality [34, 35]. A higher concentration of electron holes can enhance the overall electrical conductivity for p-type conductors. A higher concentration of oxygen vacancies can improve the oxygen ion transport properties. Both cases may have beneficial effects on the overall ORR and OER catalytic activities [33, 36, 37].

To study the effects of Ba deficiencies, the electrical conductivity of PB9CN and PB10CN were investigated. As shown in Figure 3a, PB9CN and PB10CN have sufficient and comparable electrical conductivities at intermediate temperatures ($\sim 800 \text{ S cm}^{-1}$ at $600 \text{ }^\circ\text{C}$). The similar electrical conductivity indicated that V_{Ba}'' did not have a noticeable influence on the concentration of h^\cdot . Thus, the addition of V_{Ba}'' generates V_{O}'' . To validate this, the oxygen non-stoichiometry of PB9CN and PB10CN were compared by iodometric titration and TGA. As shown in Figure 3b, PB9CN has a higher concentration of oxygen vacancies than PB10CN at temperatures below $800 \text{ }^\circ\text{C}$. To illustrate the effect of higher concentration of oxygen vacancies in PB9CN, two oxygen transport properties, i.e., surface kinetic coefficient (k) and chemical diffusion coefficient (D) were further measured using the electrical conductivity relaxation (ECR) method [38, 39]. At intermediate temperatures ($550 - 700 \text{ }^\circ\text{C}$), PB9CN exhibited better oxygen transport properties than PB10CN as shown in Figure 3c (average of two measurements). For example, at $650 \text{ }^\circ\text{C}$, the k of PB9CN and PB10CN were $4.30 \times 10^{-4} \text{ (cm s}^{-1}\text{)}$ and $1.54 \times 10^{-4} \text{ (cm s}^{-1}\text{)}$, respectively, the D of PB9CN and PB10CN were $3.03 \times 10^{-6} \text{ (cm}^2 \text{ s}^{-1}\text{)}$ and $1.72 \times 10^{-6} \text{ (cm}^2 \text{ s}^{-1}\text{)}$, respectively. Finally, the improved catalytic properties were demonstrated on SDC based symmetrical cells. Figure 3d compares the R_p of PB9CN and PB10CN symmetrical cells at $550 - 700 \text{ }^\circ\text{C}$ (average of five cells). Besides, Ba segregation of PB9CN can be further suppressed by non-stoichiometry or Ba deficiency (Figure S13) [40]. PB9CN shows improved electrochemical performance compared to PB10CN. These results prove that creating Ba deficiency dramatically improved the electrochemical performance. The optimized material, PB9CN, is thus a potential air electrode candidate for intermediate temperature SOCs.

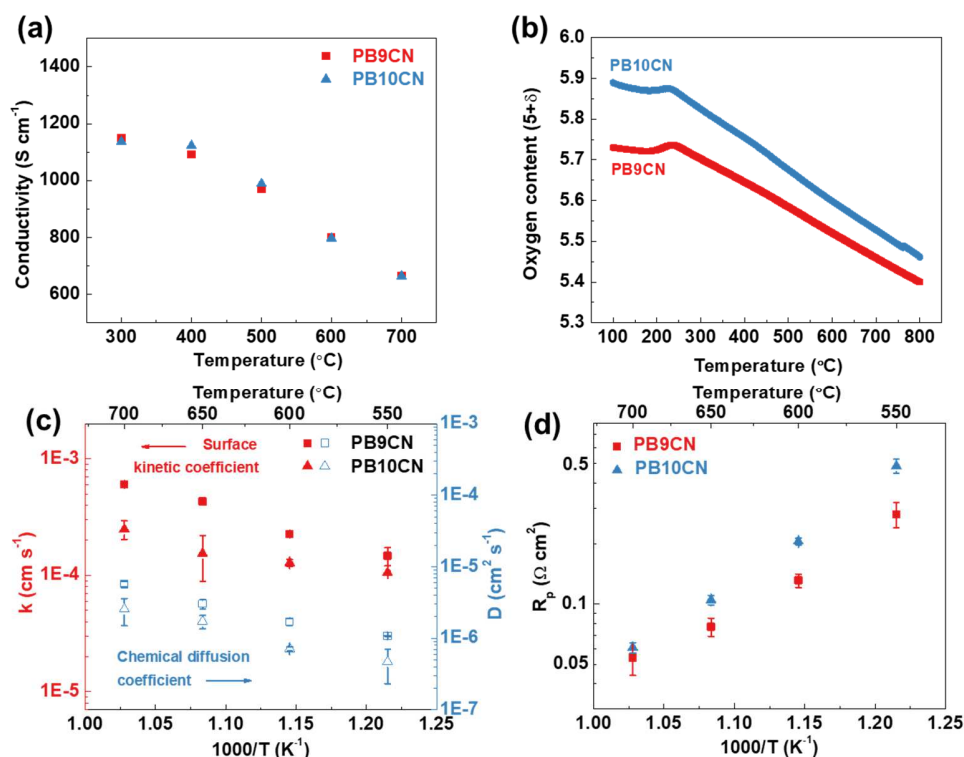


Figure 3. Improved Catalytic Activity by Tuning Ba Deficiency. (a) Electrical conductivity of PB9CN and PB10CN. (b) Oxygen non-stoichiometry of PB9CN and PB10CN. (c) Surface kinetic coefficient (k) and chemical diffusion coefficient (D) of PB9CN and PB10CN (average of two measurements). (d) Interfacial polarization resistance (R_p) of PB9CN and PB10CN based on SDC electrolyte supported symmetrical cells (average of five measurements).

3.4. Electrochemical Performance of PB9CN

The electrochemical performance of the PB9CN air electrode was examined on multiple types of SOCs (SOFCs, PCFCs, PCECs, and RePCECs). The chemical compatibility between PB9CN with an oxygen ion conducting electrolyte (GDC) and a proton conducting electrolyte (BZCYYb) were first confirmed (Figure S15). Figure S16 compares the R_p of PB9CN and other state-of-the-art air electrode materials based on SDC-supported symmetrical cells, highlighting the outstanding electrochemical activity of PB9CN. For example, at 650 °C, R_p of PB9CN is only 0.068 Ω cm², lower than that of STFC-15 (~0.089 Ω cm²) [18], BSCF-GDC core shell fibers (~0.105 Ω cm²) [41], and PBCC (~0.14 Ω cm²) [19]. The activation energy of PB9CN is 79.98 kJ mol⁻¹, which is close to the activation energy of BCFZY (79.2 kJ mol⁻¹) [20]. The low activation energy of PB9CN guarantees good ORR activity at even lower temperatures. PB9CN was then applied to GDC based single cells with a configuration of Ni-

GDC|GDC|PB9CN as shown in Figure 4a. Figure 4b shows the I-V-P curves of the single cell at 600, 550, and 500 °C. The PB9CN air electrode outperforms most of the other state-of-the-art air electrode materials or catalysts, as shown in the comparison of the peak power density of GDC or SDC based single cells in Figure 4c [42-46]. The stability of PB9CN was examined on both symmetrical cells and single cells. As shown in Figure 4d, the R_p of PB9CN does not show obvious degradation at 600 and 550 °C for over 1,000 hours. A stable operation of the GDC-based single cell for over 200 hours at 500 °C is also demonstrated in Figure 4e. PB9CN was also applied to YSZ-based cells of different sizes (Figure S17). The relatively low performance is attributed to the larger ohmic resistance of the YSZ electrolyte R_{ohm} and the larger electrode polarization resistance R_p . These results suggest that PB9CN is less active on YSZ-based cells than on the GDC- and BZCYYb-based cells. If a proper GDC buffer layer could be introduced, the PB9CN in the YSZ-based cells could be as active as in the GDC-based cells.

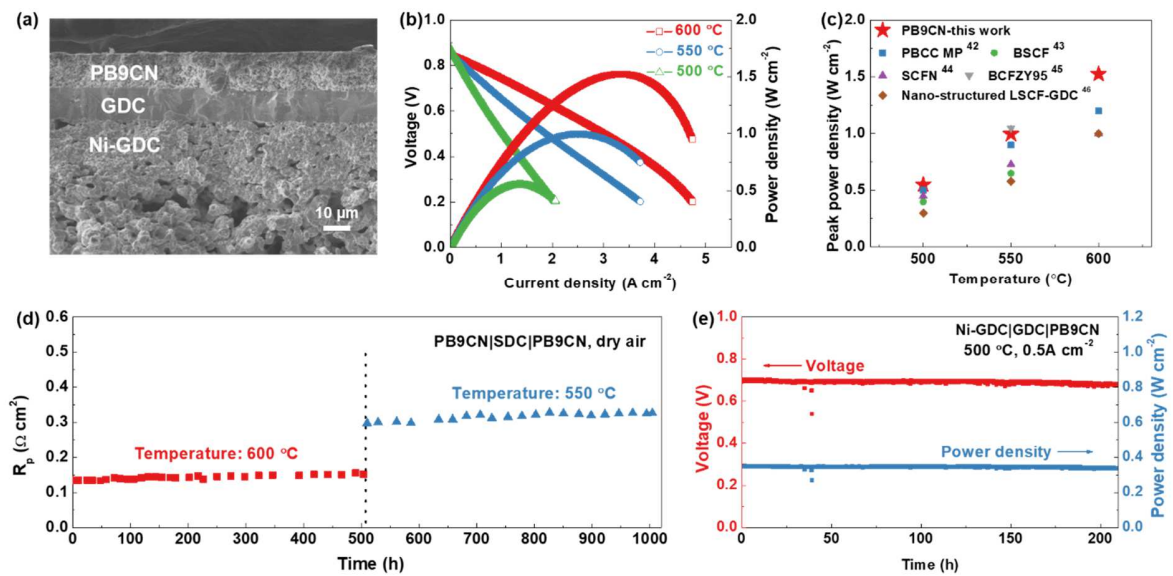


Figure 4. Application of PB9CN on oxygen ion conducting electrolytes. (a) Cross-sectional view of a single cell with a configuration of Ni-GDC | GDC | PB9CN. (b) I-V-P curves of a single cell with a configuration of Ni-GDC | GDC | PB9CN. (c) Comparison of the peak power density of GDC or SDC-based single cells with PB9CN and other state-of-the-art air electrode materials. (d) Durability of PB9CN in dry air and OCV conditions on an SDC-based symmetrical cell. (e) Durability of PB9CN on a GDC-based single cell at 500 °C.

PB9CN was also applied to a proton conducting electrolyte, i.e. BZCYYb. As shown in Figure S18, the R_p of PB9CN is comparable or lower than the best air electrode materials for PCFCs and PCECs to date when tested in humidified air (with 3 vol% H_2O) [21, 47-49]. Increasing the concentration of water didn't change the R_p of PB9CN significantly (Figure S19) [6, 8]. Figure 5a shows the cross-sectional view of a BZCYYb-based single cell with PB9CN-BZCYYb air electrode (mass ratio of PB9CN: BZCYYb=7:3). Figure 5b summarizes the electrochemical impedance spectroscopy (EIS) plots of the single cell under the OCV conditions. At temperatures below 600 °C, the R_p contributed more than the R_{ohm} to the total resistance. Figure 5c shows the I-V-P curves of the single cell under fuel cell mode at 650, 600, 550, and 500 °C. As compared in Figure 5d, the single cell performance is better than most of the reported PCFCs with other air electrode materials [4, 21, 27, 47, 50]. When operated under the electrolysis cell mode, humidified air (~3 vol% H_2O) is supplied to the air electrode and humidified H_2 (~3 vol% H_2O) is supplied to the fuel electrode. The I-V curve is shown in Figure 5e. When the applied voltage was 1.3V, the electrolysis current densities were 2.75, 1.73, and 1.07 $A\ cm^{-2}$ at 650, 600, and 550 °C, respectively, which outperforms other state-of-the-art PCECs (Table S1) [6-8, 51-55]. The stability of PB9CN against water was further examined in humidified air at 600 °C for over 500 hours (Figure S20). Figure 5f shows the reversible operation of a single cell in both fuel cell mode and electrolysis cell mode for about 50 hours. The slight degradation in the fuel cell mode is likely due to the water generated at the interface between the air electrode and the electrolyte. Figure 5g demonstrates the stable operation of the electrolysis cell at 600 °C for over 1000 hours with a degradation rate of 40 mV/1000 h. There were no obvious changes in microstructure and morphology of the electrolyte and air electrode of the single cells after operation for over 1,000 hours (Figure S21). These outstanding electrochemical performance and stability confirm the applicability of PB9CN as an air electrode material for proton conducting electrolytes as well.

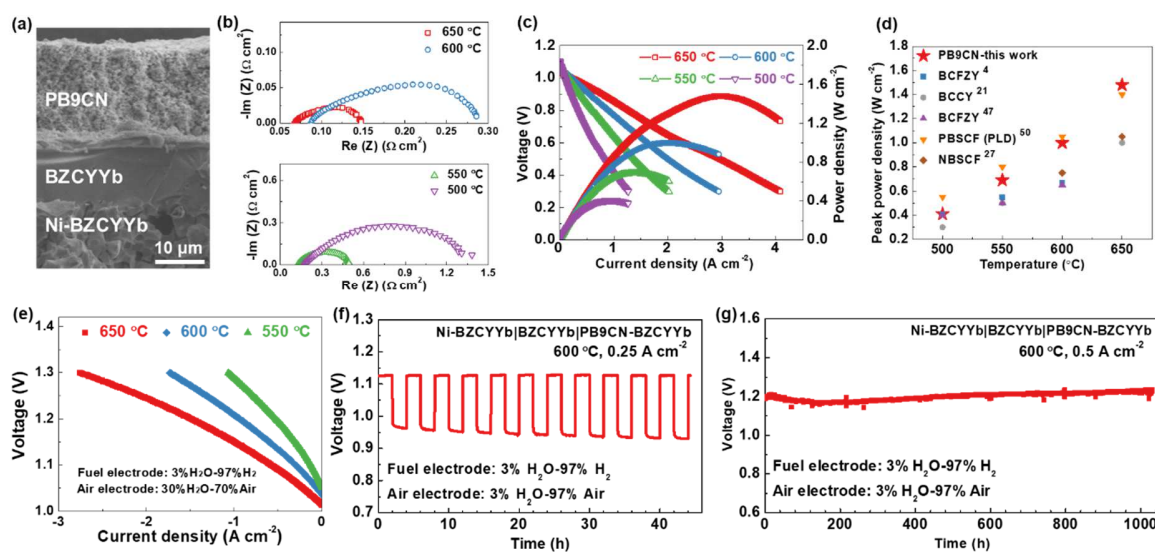


Figure 5. Application of PB9CN on proton conducting electrolytes. (a) Cross-sectional view of a single cell with a configuration of Ni-BZCYYb | BZCYYb | PB9CN-BZCYYb. (b) EIS plots of a BZCYYb-based single cell under OCV conditions. (c) I-V-P curves of a fuel cell with a configuration of Ni-BZCYYb | BZCYYb | PB9CN-BZCYYb. (d) Comparison of peak power density of BZCYYb-based single cells with PB9CN and other state-of-the-art air electrode materials. (e) I-V curve of an electrolysis cell with a configuration of Ni-BZCYYb | BZCYYb | PB9CN-BZCYYb. (f) Reversible operation of a BZCYYb-based single cell switching between fuel cell mode and electrolysis cell mode at 600 °C. (g) Durability of a BZCYYb-based electrolysis cell at 600 °C for over 1000 hours.

4. Conclusions

In conclusion, we have demonstrated a novel material PB9CN as a bi-functional air electrode for reversible solid oxide cells. The improved stability was achieved by Nb doping and the electrocatalytic activity was enhanced by Ba deficiency. The outstanding electrochemical performance and stability were demonstrated using reversible solid oxide cells based on both oxygen ion conducting electrolytes (e.g., GDC and YSZ) and proton conducting electrolytes (e.g., BZCYYb). The results presented herein show the potential of PB9CN as a bi-functional air electrode material for highly efficient energy conversion and storage devices.

Conflicts of interest

An Invention Disclosure with a number of GRTCID 8560 has been filed.

Acknowledgements

This work was supported by US Department of Energy EERE Hydrogen and Fuel Cell R&D Program under Award Number DE-EE0008439 and Phillips 66. E. L. thanks the financial support from China Scholarship Council (CSC). The calculations were performed on TianHe-1(A) at National Supercomputer Center in Tianjin.

Data availability

The raw and processed data required to reproduce these findings are available by request to the corresponding author.

References

- [1] S.D. Ebbesen, S.H. Jensen, A. Hauch, M.B. Mogensen, High temperature electrolysis in alkaline cells, solid proton conducting cells, and solid oxide cells, *Chem Rev*, 114 (2014) 10697-10734.
- [2] S. Park, Y. Shao, J. Liu, Y. Wang, Oxygen electrocatalysts for water electrolyzers and reversible fuel cells: status and perspective, *Energy & Environmental Science*, 5 (2012).
- [3] Y. Chen, B. deGlee, Y. Tang, Z. Wang, B. Zhao, Y. Wei, L. Zhang, S. Yoo, K. Pei, J.H. Kim, Y. Ding, P. Hu, F.F. Tao, M. Liu, A robust fuel cell operated on nearly dry methane at 500 °C enabled by synergistic thermal catalysis and electrocatalysis, *Nature Energy*, (2018).
- [4] C. Duan, R.J. Kee, H. Zhu, C. Karakaya, Y. Chen, S. Ricote, A. Jarry, E.J. Crumlin, D. Hook, R. Braun, N.P. Sullivan, R. O'Hayre, Highly durable, coking and sulfur tolerant, fuel-flexible protonic ceramic fuel cells, *Nature*, 557 (2018) 217-222.
- [5] S.M. Haile, Fuel cell materials and components, *Acta Materialia*, 51 (2003) 5981-6000.
- [6] C. Duan, R. Kee, H. Zhu, N. Sullivan, L. Zhu, L. Bian, D. Jennings and R. O'Hayre, Highly efficient reversible protonic ceramic electrochemical cells for power generation and fuel production, *nature Energy*, 4 (2019) 230-240.
- [7] E. Vollestad, R. Strandbakke, M. Tarach, D. Catalan-Martinez, M.L. Fontaine, D. Beeaff, D.R. Clark, J.M. Serra, T. Norby, Mixed proton and electron conducting double perovskite anodes for stable and efficient tubular proton ceramic electrolyzers, *Nat Mater*, (2019).
- [8] H. Ding, W. Wu, C. Jiang, Y. Ding, W. Bian, B. Hu, P. Singh, C.J. Orme, L. Wang, Y. Zhang, D. Ding, Self-sustainable protonic ceramic electrochemical cells using a triple conducting electrode for hydrogen and power production, *Nature Communications*, 11 (2020).
- [9] D. Ding, X. Li, S.Y. Lai, K. Gerdes, M. Liu, Enhancing SOFC cathode performance by surface modification through infiltration, *Energy & Environmental Science*, 7 (2014).
- [10] Z. Gao, L.V. Mogni, E.C. Miller, J.G. Railsback, S.A. Barnett, A perspective on low-temperature solid oxide fuel cells, *Energy & Environmental Science*, 9 (2016) 1602-1644.

- [11] J. Kim, S. Sengodan, S. Kim, O. Kwon, Y. Bu, G. Kim, Proton conducting oxides: A review of materials and applications for renewable energy conversion and storage, *Renewable and Sustainable Energy Reviews*, 109 (2019) 606-618.
- [12] C. Duan, J. Huang, N. Sullivan, R. O'Hayre, Proton-conducting oxides for energy conversion and storage, *Applied Physics Reviews*, 7 (2020).
- [13] G. Yang, C. Su, H. Shi, Y. Zhu, Y. Song, W. Zhou, Z. Shao, Toward Reducing the Operation Temperature of Solid Oxide Fuel Cells: Our Past 15 Years of Efforts in Cathode Development, *Energy & Fuels*, 34 (2020) 15169-15194.
- [14] Y. Chen, Y. Chen, D. Ding, Y. Ding, Y. Choi, L. Zhang, S. Yoo, D. Chen, B. deGlee, H. Xu, Q. Lu, B. Zhao, G. Vardar, J. Wang, H. Bluhm, E.J. Crumlin, C. Yang, J. Liu, B. Yildiz, M. Liu, A robust and active hybrid catalyst for facile oxygen reduction in solid oxide fuel cells, *Energy & Environmental Science*, 10 (2017) 964-971.
- [15] H. Téllez, J. Druce, Y.-W. Ju, J. Kilner, T. Ishihara, Surface chemistry evolution in $\text{LnBaCo}_2\text{O}_{5+\delta}$ double perovskites for oxygen electrodes, *International Journal of Hydrogen Energy*, 39 (2014) 20856-20863.
- [16] B. Wei, M. Schroeder, M. Martin, Surface Cation Segregation and Chromium Deposition on the Double-Perovskite Oxide $\text{PrBaCo}_2\text{O}_{5+\delta}$, *ACS Appl Mater Interfaces*, 10 (2018) 8621-8629.
- [17] J.-H. Kim, A. Manthiram, Layered $\text{LnBaCo}_2\text{O}_{5+\delta}$ perovskite cathodes for solid oxide fuel cells: an overview and perspective, *Journal of Materials Chemistry A*, 3 (2015) 24195-24210.
- [18] S.-L. Zhang, H. Wang, M.Y. Lu, A.-P. Zhang, L.V. Mogni, Q. Liu, C.-X. Li, C.-J. Li, S.A. Barnett, Cobalt-substituted $\text{SrTi}_{0.3}\text{Fe}_{0.7}\text{O}_{3-\delta}$: a stable high-performance oxygen electrode material for intermediate-temperature solid oxide electrochemical cells, *Energy & Environmental Science*, 11 (2018) 1870-1879.
- [19] Y. Chen, S. Yoo, Y. Choi, J.H. Kim, Y. Ding, K. Pei, R. Murphy, Y. Zhang, B. Zhao, W. Zhang, H. Chen, Y. Chen, W. Yuan, C. Yang, M. Liu, A highly active, CO_2 -tolerant electrode for the oxygen reduction reaction, *Energy & Environmental Science*, 11 (2018) 2458-2466.
- [20] C. Duan, D. Hook, Y. Chen, J. Tong, R. O'Hayre, Zr and Y co-doped perovskite as a stable, high performance cathode for solid oxide fuel cells operating below 500 °C, *Energy & Environmental Science*, 10 (2017) 176-182.
- [21] Y. Song, Y. Chen, W. Wang, C. Zhou, Y. Zhong, G. Yang, W. Zhou, M. Liu, Z. Shao, Self-Assembled Triple-Conducting Nanocomposite as a Superior Protonic Ceramic Fuel Cell Cathode, *Joule*, (2019).
- [22] G. Kresse, Efficient iterative schemes for ab initio total-energy calculations using a plane-wave basis set, *PHYSICAL REVIEW B*, 54 (1996) 11169-11186.
- [23] K.B. John P. Perdew, Matthias Ernzerhof, Generalized Gradient Approximation Made Simple, *PHYSICAL REVIEW LETTERS*, 77 (1996) 3865-3868.
- [24] M. Methfessel, A.T. Paxton, High-precision sampling for Brillouin-zone integration in metals, *Phys Rev B Condens Matter*, 40 (1989) 3616-3621.
- [25] H.J. Monkhorst, J.D. Pack, Special points for Brillouin-zone integrations, *Physical Review B*, 13 (1976) 5188-5192.
- [26] S. Choi, S. Yoo, J. Kim, S. Park, A. Jun, S. Sengodan, J. Kim, J. Shin, H.Y. Jeong, Y. Choi, G. Kim, M. Liu, Highly efficient and robust cathode materials for low-temperature solid oxide fuel cells: $\text{PrBa}_{0.5}\text{Sr}_{0.5}\text{Co}_{2-x}\text{Fe}_x\text{O}_{5+\delta}$, *Sci Rep*, 3 (2013) 2426.
- [27] J. Kim, S. Sengodan, G. Kwon, D. Ding, J. Shin, M. Liu, G. Kim, Triple-conducting layered perovskites as cathode materials for proton-conducting solid oxide fuel cells, *ChemSusChem*, 7 (2014) 2811-2815.
- [28] M.N. Feifei Dong, Yubo Chen, Dengjie Chen, Moses O. Tad and Zongping Shao, Structural and oxygen-transport studies of double perovskites $\text{PrBa}_{1-x}\text{Co}_2\text{O}_{5+\delta}$ ($x = 0.00, 0.05, \text{ and } 0.10$) toward their application as superior oxygen reduction electrodes, *Journal of Materials Chemistry A*, 2 (2014) 20520.
- [29] K. Zhang, L. Ge, R. Ran, Z. Shao, S. Liu, Synthesis, characterization and evaluation of cation-ordered $\text{LnBaCo}_2\text{O}_{5+\delta}$ as materials of oxygen permeation membranes and cathodes of SOFCs, *Acta Materialia*, 56 (2008) 4876-4889.

- [30] J. Druce, H. Téllez, M. Burriel, M.D. Sharp, L.J. Fawcett, S.N. Cook, D.S. McPhail, T. Ishihara, H.H. Brongersma, J.A. Kilner, Surface termination and subsurface restructuring of perovskite-based solid oxide electrode materials, *Energy Environ. Sci.*, 7 (2014) 3593-3599.
- [31] N. Tsvetkov, Q. Lu, L. Sun, E.J. Crumlin, B. Yildiz, Improved chemical and electrochemical stability of perovskite oxides with less reducible cations at the surface, *Nat Mater*, 15 (2016) 1010-1016.
- [32] R. Ren, Z. Wang, C. Xu, W. Sun, J. Qiao, D.W. Rooney, K. Sun, Tuning the defects of the triple conducting oxide $\text{BaCo}_{0.4}\text{Fe}_{0.4}\text{Zr}_{0.1}\text{Y}_{0.1}\text{O}_{3-6}$ perovskite toward enhanced cathode activity of protonic ceramic fuel cells, *Journal of Materials Chemistry A*, 7 (2019) 18365-18372.
- [33] W. Tang, H. Ding, W. Bian, W. Wu, W. Li, X. Liu, J.Y. Gomez, C.Y. Regalado Vera, M. Zhou, D. Ding, Understanding of A-site deficiency in layered perovskites: promotion of dual reaction kinetics for water oxidation and oxygen reduction in protonic ceramic electrochemical cells, *Journal of Materials Chemistry A*, 8 (2020) 14600-14608.
- [34] M. Liu, Distributions of Charged Defects in Mixed Ionic-Electronic Conductors, *J. Electrochem. Soc.*, 144 (1997) 1813-1834.
- [35] M.L. Zhonglin Wu, Modelling of ambipolar transport properties of composite mixed ionic-electronic conductors, *Solid State Ionics*, 93 (1997) 65-84.
- [36] B. Zhao, L. Zhang, D. Zhen, S. Yoo, Y. Ding, D. Chen, Y. Chen, Q. Zhang, B. Doyle, X. Xiong, M. Liu, A tailored double perovskite nanofiber catalyst enables ultrafast oxygen evolution, *Nat Commun*, 8 (2017) 14586.
- [37] K.J.M. Jin Suntivich, Hubert A. Gasteiger, John B. Goodenough, Yang Shao-Horn, A Perovskite Oxide Optimized for Oxygen Evolution Catalysis from Molecular Orbital Principles, *Science*, 334 (2011) 1383-1385.
- [38] I.Y.a.T. Hikita, Precise Determination of the Chemical Diffusion Coefficient of Calcium-Doped Lanthanum Chromites by Means of Electrical Conductivity Relaxation, *J. Electrochem. Soc.*, 141 (1994) 1268-1273.
- [39] I.Y.a.M. Hishinuma, Electrical conductivity and chemical diffusion coefficient of Sr-doped lanthanum chromites, *Solid State Ionics*, 80 (1995) 141-150.
- [40] K. Chen, S.P. Jiang, Surface Segregation in Solid Oxide Cell Oxygen Electrodes: Phenomena, Mitigation Strategies and Electrochemical Properties, *Electrochemical Energy Reviews*, 3 (2020) 730-765.
- [41] J.G. Lee, J.H. Park, Y.G. Shul, Tailoring gadolinium-doped ceria-based solid oxide fuel cells to achieve 2 W cm^{-2} at 550 degrees C, *Nat Commun*, 5 (2014) 4045.
- [42] Y. Chen, Y. Choi, S. Yoo, Y. Ding, R. Yan, K. Pei, C. Qu, L. Zhang, I. Chang, B. Zhao, Y. Zhang, H. Chen, Y. Chen, C. Yang, B. deGlee, R. Murphy, J. Liu, M. Liu, A Highly Efficient Multi-phase Catalyst Dramatically Enhances the Rate of Oxygen Reduction, *Joule*, 2 (2018) 938-949.
- [43] Z. Shao, S. Haile, A high-performance cathode for the next generation of solid-oxide fuel cells, *Nature*, 431 (2004) 170-173.
- [44] Y. Song, Y. Chen, M. Xu, W. Wang, Y. Zhang, G. Yang, R. Ran, W. Zhou, Z. Shao, A Cobalt-Free Multi-Phase Nanocomposite as Near-Ideal Cathode of Intermediate-Temperature Solid Oxide Fuel Cells Developed by Smart Self-Assembly, *Adv Mater*, (2020) e1906979.
- [45] X. Kuai, G. Yang, Y. Chen, H. Sun, J. Dai, Y. Song, R. Ran, W. Wang, W. Zhou, Z. Shao, Boosting the Activity of $\text{BaCo}_{0.4}\text{Fe}_{0.4}\text{Zr}_{0.1}\text{Y}_{0.1}\text{O}_{3-6}$ Perovskite for Oxygen Reduction Reactions at Low-to-Intermediate Temperatures through Tuning B-Site Cation Deficiency, *Advanced Energy Materials*, (2019).
- [46] C. Ding, T. Hashida, High performance anode-supported solid oxide fuel cell based on thin-film electrolyte and nanostructured cathode, *Energy & Environmental Science*, 3 (2010).
- [47] C. Duan, J. Tong, M. Shang, S. Nikodemski, M. Sanders, S. Ricote, A. Almansoori, R. O'Hayre, Readily processed protonic ceramic fuel cells with high performance at low temperatures, *Science*, 349 (2015) 1321-1326.

- [48] A. Grimaud, F. Mauvy, J.M. Bassat, S. Fourcade, L. Rocheron, M. Marrony, J.C. Grenier, Hydration Properties and Rate Determining Steps of the Oxygen Reduction Reaction of Perovskite-Related Oxides as H⁺-SOFC Cathodes, *Journal of The Electrochemical Society*, 159 (2012) B683-B694.
- [49] Y. Lin, R. Ran, Y. Zheng, Z. Shao, W. Jin, N. Xu, J. Ahn, Evaluation of Ba_{0.5}Sr_{0.5}Co_{0.8}Fe_{0.2}O_{3-δ} as a potential cathode for an anode-supported proton-conducting solid-oxide fuel cell, *Journal of Power Sources*, 180 (2008) 15-22.
- [50] S. Choi, C.J. Kucharczyk, Y. Liang, X. Zhang, I. Takeuchi, H.-I. Ji, S.M. Haile, Exceptional power density and stability at intermediate temperatures in protonic ceramic fuel cells, *Nature Energy*, 3 (2018) 202-210.
- [51] S. Choi, T. Davenport, S. Haile, Protonic ceramic electrochemical cells for hydrogen production and electricity generation: exceptional reversibility, stability, and demonstrated faradaic efficiency, *Energy Environ. Sci.*, 12 (2019) 206-215.
- [52] W. Wu, H. Ding, Y. Zhang, Y. Ding, P. Katiyar, P.K. Majumdar, T. He, D. Ding, 3D Self-Architected Steam Electrode Enabled Efficient and Durable Hydrogen Production in a Proton-Conducting Solid Oxide Electrolysis Cell at Temperatures Lower Than 600 °C, *Advanced Science*, (2018).
- [53] D. Huan, N. Shi, L. Zhang, W. Tan, Y. Xie, W. Wang, C. Xia, R. Peng, Y. Lu, New, Efficient, and Reliable Air Electrode Material for Proton-Conducting Reversible Solid Oxide Cells, *ACS Appl Mater Interfaces*, 10 (2018) 1761-1770.
- [54] J. Kim, A. Jun, O. Gwon, S. Yoo, M. Liu, J. Shin, T.-H. Lim, G. Kim, Hybrid-solid oxide electrolysis cell: A new strategy for efficient hydrogen production, *Nano Energy*, 44 (2018) 121-126.
- [55] W. Li, B. Guan, L. Ma, S. Hu, N. Zhang, X. Liu, High performing triple-conductive Pr₂NiO_{4+δ} anode for proton-conducting steam solid oxide electrolysis cell, *Journal of Materials Chemistry A*, 6 (2018) 18057-18066.

